

# Journal of Biomedical Optics

BiomedicalOptics.SPIEDigitalLibrary.org

## ***In vivo* subdiffuse scanning laser oximetry of the human retina**

Mathi Damodaran  
Arjen Amelink  
Fabio Feroldi  
Benjamin Lochocki  
Valentina Davidoiu  
Johannes F. de Boer

**SPIE.**

Mathi Damodaran, Arjen Amelink, Fabio Feroldi, Benjamin Lochocki, Valentina Davidoiu, Johannes F. de Boer, "*In vivo* subdiffuse scanning laser oximetry of the human retina," *J. Biomed. Opt.* **24**(9), 096009 (2019), doi: 10.1117/1.JBO.24.9.096009.

# *In vivo* subdiffuse scanning laser oximetry of the human retina

Mathi Damodaran,<sup>a,\*†</sup> Arjen Amelink,<sup>b</sup> Fabio Feroldi,<sup>a</sup> Benjamin Lochocki,<sup>a</sup> Valentina Davidoiu,<sup>a,†</sup> and Johannes F. de Boer<sup>a,c</sup>

<sup>a</sup>Vrije Universiteit Amsterdam, LaserLaB, Department of Physics and Astronomy, Amsterdam, The Netherlands

<sup>b</sup>Netherlands Organization for Applied Scientific Research TNO, Department of Optics, Delft, The Netherlands

<sup>c</sup>Amsterdam UMC, Ophthalmology Department, Amsterdam, The Netherlands

**Abstract.** Scanning laser ophthalmoscopes (SLOs) have the potential to perform high speed, high contrast, functional imaging of the human retina for diagnosis and follow-up of retinal diseases. Commercial SLOs typically use a monochromatic laser source or a superluminescent diode for imaging. Multispectral SLOs using an array of laser sources for spectral imaging have been demonstrated in research settings, with applications mainly aiming at retinal oxygenation measurements. Previous SLO-based oximetry techniques are predominantly based on wavelengths that depend on laser source availability. We describe an SLO system based on a supercontinuum (SC) source and a double-clad fiber using the single-mode core for illumination and the larger inner cladding for quasi-confocal detection to increase throughput and signal-to-noise ratio. A balanced detection scheme was implemented to suppress the relative intensity noise of the SC source. The SLO produced dual wavelength, high-quality images at 10 frames/s with a maximum 20 deg imaging field-of-view with any desired combination of wavelengths in the visible spectrum. We demonstrate SLO-based dual-wavelength oximetry in vessels down to 50  $\mu\text{m}$  in diameter. Reproducibility was demonstrated by performing three different imaging sessions of the same volunteer, 8 min apart. Finally, by performing a wavelength sweep between 485 and 608 nm, we determined, for our SLO geometry, an approximately linear relationship between the effective path length of photons through the blood vessels and the vessel diameter. © The Authors. Published by SPIE under a Creative Commons Attribution 4.0 Unported License. Distribution or reproduction of this work in whole or in part requires full attribution of the original publication, including its DOI. [DOI: [10.1117/1.JBO.24.9.096009](https://doi.org/10.1117/1.JBO.24.9.096009)]

Keywords: retinal oximetry; scanning laser ophthalmoscope; hemoglobin; oxygen saturation; hyperspectral imaging; path length.

Paper 190209R received Jun. 22, 2019; accepted for publication Sep. 9, 2019; published online Sep. 30, 2019.

## 1 Introduction

Measuring the amount of oxygenated and deoxygenated hemoglobin present in the retinal vessels is potentially very valuable to detect and monitor retinal diseases. Oxygen saturation in the retinal vasculature is an important indicator of retinal health.<sup>1,2</sup> Several studies have investigated and found associations between retinal pathologies and retinal vessel oxygen saturation.<sup>3–9</sup> Moreover, retinal vessel oxygen saturation has also been linked to neurodegenerative diseases.<sup>10–12</sup> Various imaging techniques have been employed in the past to measure retinal oxygen saturation,<sup>13–22</sup> and recently emerging techniques have enabled oximetry to be applied in a variety of *in vivo* applications.<sup>23–25</sup> Nevertheless, the vast majority of retinal oximetry studies use a fundus camera-based approach, which has a limited spatial resolution and provides insufficient contrast to perform oximetry in retinal microvessels smaller than  $\sim 100 \mu\text{m}$ . However, it is in the smaller microvessels that the oxygen saturation is expected to decrease in response to local increased metabolic demand or decreased oxygen delivery capacity. The larger retinal vessels that can be resolved by fundus cameras are expected to be much less sensitive to local changes in tissue metabolic demand or microvascular dysfunction; therefore, the microvasculature provides the most clinically relevant information on local tissue metabolic status. This

motivates the development of a scanning-laser-ophthalmoscope (SLO) based oximeter, capable of resolving the oxygen saturation in vessels as small as  $\sim 50 \mu\text{m}$ .

We have recently shown that the signal-to-noise ratio (SNR) of the retinal image strongly influences the accuracy of retinal oximetry.<sup>26</sup> Since the permissible light exposure of the retina is limited in order to prevent injury, it is important to use the allowable light budget efficiently. This implies that imaging should be performed at dedicated wavelength bands, providing the highest SNR for the available light budget. Additionally, averaging of multiple scans of the retina at each wavelength may be necessary to reach a target SNR required to achieve the desired oxygen saturation accuracy.

In this paper, we demonstrate the next-generation SLO-based retinal oximeter with optimized wavelengths and throughput, which can measure retinal oxygenation in vessels down to  $\sim 50 \mu\text{m}$  diameter. We will first briefly describe the method to select an optimum wavelength for retinal oximetry by taking into account the error on the measured intensities in the retina, the pigment packing effect, the maximum permissible power that can be used for retinal illumination, and the quantum efficiency of the detector. Then, we describe the design of an SLO that employs a supercontinuum (SC) source for producing continuous, high contrast images at any desired wavelength from 484 to 700 nm at a speed of 10 frames/s. Balanced detection was implemented to suppress the relative intensity noise (RIN) of the SC source that required to achieve a sufficiently high SNR in the retinal images. Finally, to establish the imaging capabilities of the device, healthy volunteers were imaged.

\*Address all correspondence to Mathi Damodaran, E-mail: [mathid@outlook.com](mailto:mathid@outlook.com)

†Present address: Philips Research, High Tech Campus, 5656 AE Eindhoven, The Netherlands

We demonstrate the effect of including an achromatizing lens in the setup to cancel the chromatic aberrations of the eye. Finally, we demonstrate that the extracted oxygen saturation of the smaller retinal vessels is reproducible and within expected physiological ranges.

## 2 Methods

### 2.1 Wavelength Selection for Dual Wavelength Retinal Oximetry

Oxygenation is typically assessed by imaging the retinal vessels at different wavelengths using multispectral imaging techniques, where the choice of wavelengths will affect the achievable measurement accuracy. In an earlier publication, we provided a detailed explanation and calculation of retinal oximetry with and without the pigment packing effect.<sup>26</sup> Here, we present a summary of the calculations but now without assuming the use of an isosbestic wavelength for oximetry, as was done in our previous paper. Furthermore, we will account for the maximum permissible power that can be used for retinal illumination and the quantum efficiency of the detector in the calculations.

Let  $I(\bar{x}_b, \lambda)$  and  $I(\bar{x}_t, \lambda)$  be the recorded intensities in the retinal image at the center of the blood vessel and adjacent tissue location, respectively, at a wavelength  $\lambda$  and for equal illumination intensity at both locations. The relative optical density  $OD_\lambda$  of the blood vessel location compared to the surrounding tissue can be written as follows:

$$OD_\lambda = \ln \left[ \frac{I(\bar{x}_t, \lambda)}{I(\bar{x}_b, \lambda)} \right] = \langle L_{\text{eff}}(\lambda) \rangle \cdot [S \cdot \mu_a^{\text{HbO}_2}(\lambda) + (1 - S) \cdot \mu_a^{\text{Hb}}(\lambda)] + G(\lambda), \quad (1)$$

where the attenuation of the reflected light due to the blood within  $\bar{x}_b$  is governed by modified Beer–Lambert’s law,<sup>27,28</sup> with  $\langle L_{\text{eff}}(\lambda) \rangle$ , the effective path length of photons traveling through the probed volume before reaching the detector. The absorption coefficients of oxy- and deoxyhemoglobin are given by  $\mu_a^{\text{HbO}_2}(\lambda)$  and  $\mu_a^{\text{Hb}}(\lambda)$ , respectively, assuming a concentration of hemoglobin of 15 g/dL.  $G(\lambda)$  is a factor, which accounts for any apparent increase or decrease in the ODs purely due to scattering differences within the volumes  $\bar{x}_b$  and  $\bar{x}_t$ . We define the ratio of ODs at two wavelengths  $\lambda_1$  and  $\lambda_2$  as follows:

$$\rho_{\lambda_1|\lambda_2} = \frac{OD_{\lambda_1}}{OD_{\lambda_2}}. \quad (2)$$

We can then write the saturation (i.e., the fraction of the oxygenated hemoglobin concentration to the total concentration of hemoglobin) as follows:<sup>26</sup>

$$S_{\lambda_1|\lambda_2} = \frac{\rho_{\lambda_1|\lambda_2} \cdot \mu_a^{\text{Hb}}(\lambda_2) - \mu_a^{\text{Hb}}(\lambda_1)}{[\mu_a^{\text{Hb}}(\lambda_2) - \mu_a^{\text{HbO}_2}(\lambda_2)] \cdot \rho_{\lambda_1|\lambda_2} + [\mu_a^{\text{HbO}_2}(\lambda_1) - \mu_a^{\text{Hb}}(\lambda_1)]} + \alpha \cdot G, \quad (3)$$

where the factor  $\alpha * G$  ( $\alpha = (\rho - 1) / \langle L_{\text{eff}} \rangle \cdot \nu \cdot [\mu_a^{\text{HbO}_2}(\lambda_2)] - [\mu_a^{\text{Hb}}(\lambda_2)] \cdot \rho + \{\mu_a^{\text{HbO}_2}(\lambda_1) - [\mu_a^{\text{Hb}}(\lambda_1)]\}$ ) is an offset, if any, to the saturation due to scattering. The error on the saturation,  $\Delta S$ , is given by

$$\Delta S = (dS/d\rho) * \Delta\rho, \quad (4)$$

where the error in  $\rho_{\lambda_1|\lambda_2}$ ,  $\Delta\rho$  is given by the underlying error in the ODs resulting from the error in recorded intensities [please refer to Damodaran et al.<sup>26</sup> for mathematical expressions relating  $\Delta S$  to  $\Delta I$ ]. The error in saturation can be calculated using Eq. (4). The result is plotted in Fig. 1 for different wavelength combinations, where  $\lambda \in (460 \text{ to } 650) \text{ nm}$  and the standard error on the mean recorded intensity values ( $\Delta I/I$ ) was assumed to be 1%. This figure shows the wavelength combinations that give the smallest saturation errors for a given saturation level. Figure 1 depends on Eq. (3), which is correct for a large blood vessel superficially present in the retina with a diameter comparable to the collection area. In the case of a small blood vessel embedded in the scattering retinal tissue that is illuminated with a narrow beam, and when the collection aperture is much larger than the illumination aperture and the blood vessel diameter, then the blood vessel occupies only a small portion of the total probed volume. Hence, the pigment packing effect should be considered and incorporated into the ODs.<sup>26,29,30</sup> Equation (3) can then be written as follows:

$$S_{\lambda_1|\lambda_2,pp} = \frac{\rho_{\lambda_1|\lambda_2} \cdot \frac{C_{\lambda_2}}{C_{\lambda_1}} \cdot \mu_a^{\text{Hb}}(\lambda_2) - \mu_a^{\text{Hb}}(\lambda_1)}{[\mu_a^{\text{Hb}}(\lambda_2) - \mu_a^{\text{HbO}_2}(\lambda_2)] \cdot \rho_{\lambda_1|\lambda_2} \cdot \frac{C_{\lambda_2}}{C_{\lambda_1}} + [\mu_a^{\text{HbO}_2}(\lambda_1) - \mu_a^{\text{Hb}}(\lambda_1)]} + \alpha \cdot G, \quad (5)$$

where  $C_\lambda$  is the correction factor to include the pigment packing effect and  $\alpha * G$   $\{\alpha = (\rho - 1) / \langle L_{\text{eff}} \rangle \cdot \nu \cdot [\mu_a^{\text{HbO}_2}(\lambda_2)] - [\mu_a^{\text{Hb}}(\lambda_2)] \cdot \rho + [\mu_a^{\text{HbO}_2}(\lambda_1) - [\mu_a^{\text{Hb}}(\lambda_1)]]\}$  is an offset due to scattering. It can be observed that if the ratio of correction factors  $C_{\lambda_2}/C_{\lambda_1}$  in Eq. (5) is 1; Eq. (5) reduces to Eq. (3) i.e.,  $C_{\lambda_2}/C_{\lambda_1} \simeq 1 \Rightarrow S_{\lambda_1|\lambda_2} \simeq S_{\lambda_1|\lambda_2,pp}$ .

Figure 2(a) shows an ensemble  $\Delta S$ , where weights of 0.4, 0.6, 0.8, 1.0, and 1.0 were applied to the five different saturation graphs  $S = 0.00, 0.25, 0.50, 0.75,$  and  $1.00$  in Fig. 1, respectively. The weights were chosen to favor the more physiologically relevant, health range of oxygen saturation.<sup>31</sup> Figure 2(b) shows the difference in calculated saturation with and without the pigment packing effect defined as the saturation offset,  $S_{\text{offset}}$  ( $S_{\text{offset}} = S_{\lambda_1|\lambda_2} - S_{\lambda_1|\lambda_2,pp}$ ) due to the pigment packing effect when the same weights were applied. Figure 2(c) shows the addition of the saturation offset and the saturation error for wavelengths  $\lambda_1, \lambda_2 \in [450 \text{ to } 650]$ , respectively. Finally, Fig. 2(d) shows Fig. 2(c) corrected for the wavelength-dependent maximum permissible exposure (MPE) prescribed for 30,000 s of continuous single-point exposure<sup>32</sup> (see Fig. 15 in Sec. 5) and responsivity of the detector across the wavelengths.<sup>33</sup> The  $\Delta I/I$  value was 1% for the MPE and responsivity at 600 nm and increases linearly for decreasing MPE and responsivity as a function of the wavelength to get Fig. 2(d). For example, at 460 nm, the MPE normalized on the MPE for  $\lambda \geq 500 \text{ nm}$  was 0.1 and the responsivity normalized on the responsivity at 600 nm was 0.7 and hence, the  $\Delta I/I$  was adjusted to 14.3%. Based on Fig. 2(d), 498- and 594-nm wavelengths were chosen for oximetry estimation.

### 2.2 System Design

The scanning laser oximeter setup was an adaptation of our previous design,<sup>26</sup> with the aim to optimize the SNR of our imaging system. A schematic layout of the system is shown in Fig. 3. The

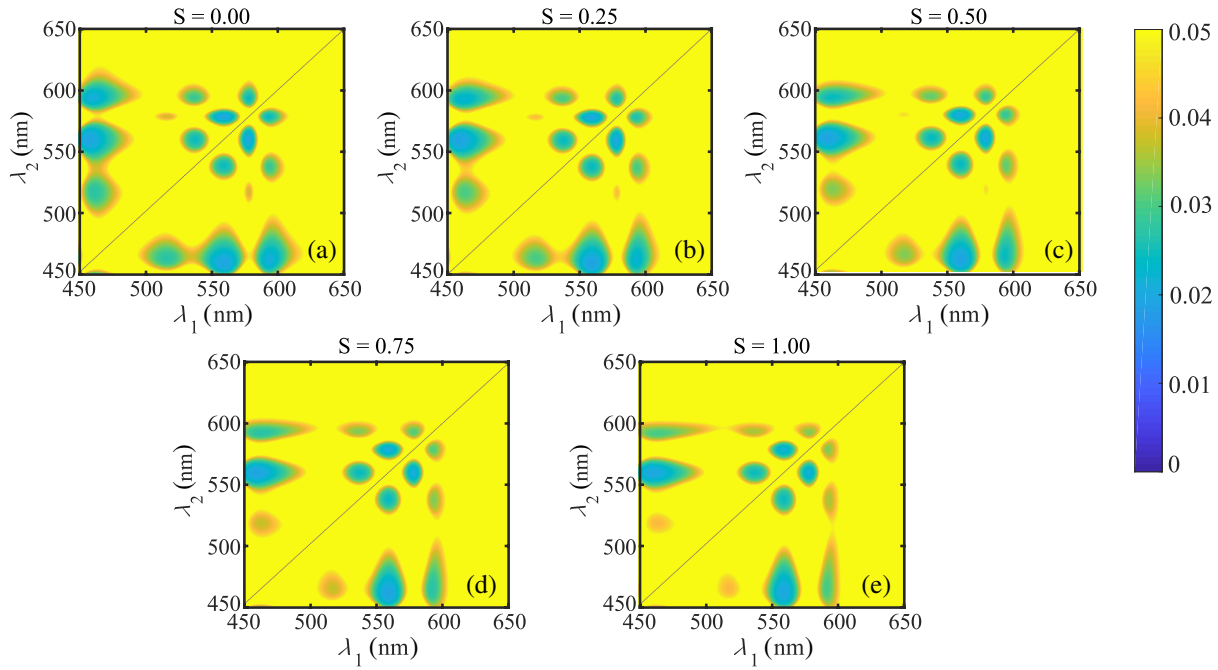


**Fig. 1** (a)–(e) *In silico* analysis of saturation error  $\Delta S$  for different saturation levels and wavelength combinations for  $\lambda_1, \lambda_2 \in (450 \text{ to } 650) \text{ nm}$ . The standard error on the mean recorded intensity values ( $\Delta I/I$ ) was assumed to be 1%. All values of  $\Delta S > 0.05$  were set to 0.05.

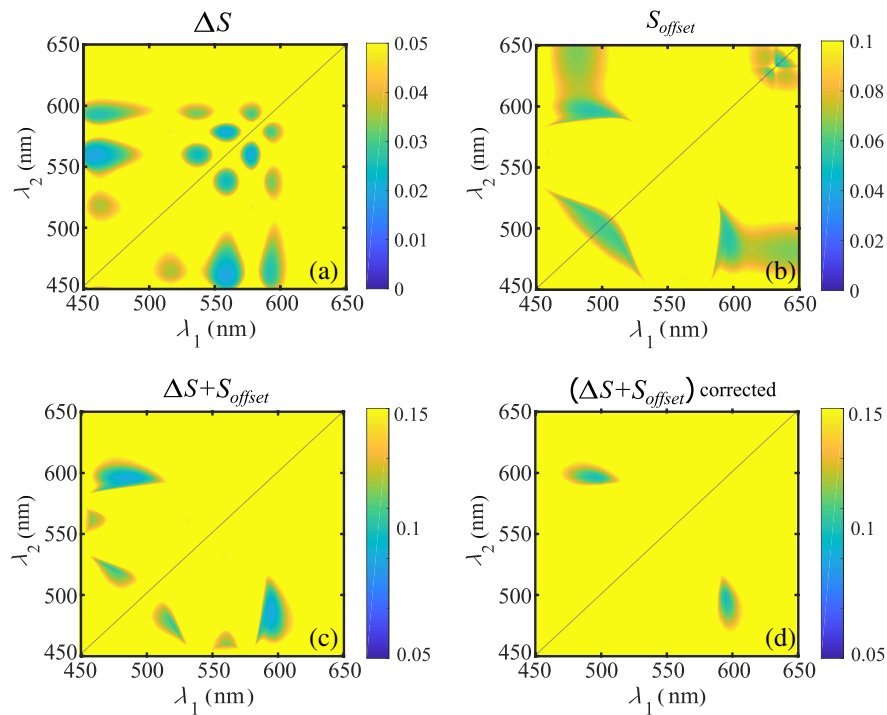


**Fig. 2** *In silico* analysis of saturation error and saturation offset. (a) Saturation error  $\Delta S$  for different wavelength combinations for  $\lambda_1, \lambda_2 \in (450 \text{ to } 650) \text{ nm}$ . The standard error on the mean recorded intensity values ( $\Delta I/I$ ) was assumed to be 1%. All values of  $\Delta S > 0.05$  are shown as 0.05. (b) Calculated saturation difference with and without pigment packing effect shown as an offset ( $S_{\text{offset}} = S_{\lambda_1|\lambda_2} - S_{\lambda_1|\lambda_2,pp}$ ) for a 50- $\mu\text{m}$  diameter blood vessel. Values of  $S_{\text{offset}} > 0.1$  are shown as 0.1. (c) Addition of the saturation offset and the saturation error for different wavelength combinations. The color bar has a range from 0.05 to 0.15. (d) Addition of saturation offset and saturation error corrected for the MPE prescribed for 30,000 s of continuous single-point exposure (see Sec. 5), and quantum efficiency of the detector across the wavelengths.

light from an SC source (EXU-6, NKT Photonics A/S, Birkerød, Denmark) was filtered using a tunable filter (Select, NKT Photonics A/S). A 90:10 fused single-mode 460-HP fiber coupler (TW560R2A2, Thorlabs GmbH, Germany) was used to send 10% of the light into detection module II for continuous laser power monitoring and balanced detection (see Sec. 2.3). The core of the double-clad fiber (DCF) in port S of the DCFC<sup>34,35</sup> was excited using the 90% port of the splitter. About 94% (transmission measured at 550 nm) of this light reached the port A of the DCFC. A reflective fiber collimator (RC02APC-P01, Thorlabs GmbH) was used to collimate the

fiber output from port A into a 2.2 mm beam. This beam size was optimum for two reasons: (i) The beam size was small enough that the beam is not clipped in the pupil of the subject even with the expected pupil constriction due to bright visible radiation. (ii) This beam size was close to the optimum pupil size for lateral resolution.<sup>36</sup> A dichroic mirror (D3, long pass cutoff 700 nm) was used to prevent any residual pump light of the SC from entering the rest of the system. A custom-made dispersion compensating lens (DCL) (Shanghai optics Inc., H-FK61 and K4A,  $f = 1800$  mm) was placed in the common beam path to compensate for the longitudinal focal shift arising from the

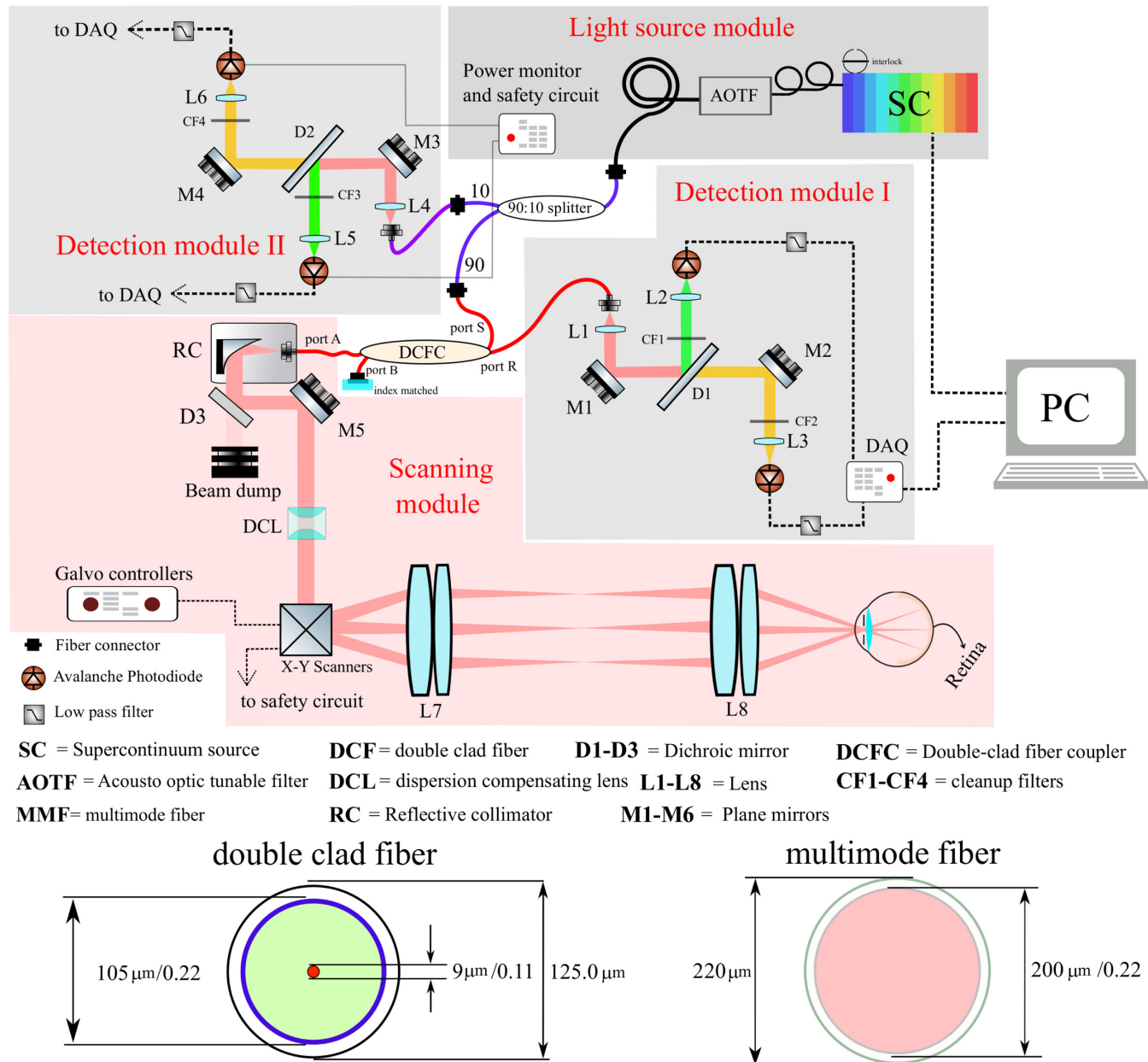


**Fig. 3** Schematic sketch of the scanning laser oximeter showing the various components. The abbreviated components are described in the legend. The light from port A of the DCFC was collimated using RC into a 2.2 mm beam. The reflected signal from the retina was collected using the cladding of the DCF with a diameter of 105 μm and a numerical aperture (NA) of 0.22. This light is coupled on to the MMF with a diameter of 200 μm and an NA of 0.22. Thus, the illumination pinhole size is 9 μm and the detection pinhole size is 105 μm. The maximum collection beam diameter of RC was 8 mm. However, the limiting aperture in the optical setup is the pupil of the subject.

chromatic aberration of the human eye.<sup>37</sup> A combination of a 2.56-kHz resonant scanner (5.12 kHz line rate by utilizing both sides of scanner sweep) (EPOC., Glendale, New York, United States), and a 10-Hz galvanometer mirror (Cambridge Technology, Bedford, Massachusetts, United States) placed close to each other were used to achieve an imaging throughput of 5.12 million pixels/s (10 frames/s 512 lines/frame 1000 pixels/line). A 1:1 telescope consisting of achromatic doublet pairs was used to relay a point approximately in the middle of the two scanning mirrors onto the pupil of the eye. The reflected and scattered light from the retina was then collected using the inner cladding of the DCF in port A. About 63% (transmission measured at 550 nm) of the collected light is then coupled into the multimode fiber. The fiber cross-section of the DCF and the MMF in the DCF coupler is also shown in Fig. 3.

The detection modules consist of a collimating lens (L1 and L4,  $f = 18$  mm), a dichroic mirror (D1 and D2, long pass cutoff 532 nm), and two focusing lenses (L2, L3, L5, and L6,  $f = 25$  mm) focusing the spectrally separated light on the active area of avalanche photodiodes (APD) (APD410A2, Thorlabs GmbH). Two clean-up filters (CF1, CF3: bandpass  $470 \pm 50$  nm, CF2, CF4: long pass 532 nm) were placed just before the focusing lenses to avoid any contribution of light from an unintended wavelength. The detectors in both the detection modules were connected to a 12-bit digitizer (NI-PCI6115, 10 million samples/s/channel, National Instruments, Austin, Texas). The signals from the four detection modules were sampled using four parallel channels of this digitizer running on a single clock. Port B of the DCF coupler was placed in a medium, whose index was matching the core index of the MMF to suppress the back reflection from the exit surface of the fiber facet from entering the detection module I.

### 2.3 Balanced Detection to Increase the Signal-to-Noise Ratio

Spectrally filtering an SC light source provides an excellent wavelength-flexible alternative to the existing approaches of multispectral imaging. However, in an SC light source such as the EXU-6 used in the setup shown in Fig. 3, the generation of a large optical bandwidth through nonlinear processes<sup>38,39</sup> results in high RIN compared to traditional sources, such as LEDs, lasers, and superluminescent diodes. The fundamental noise limitation of an SC source is described well by Corwin et al.<sup>40</sup> The pulse-to-pulse intensity variations in the SC source amounts to the RIN. In principle, RIN can be suppressed by averaging more pulses within the integration time of the detector. The EXU-6 has a repetition rate of 78 MHz, and given the short integration times of our SLO, ( $\sim 380$  ns) only 30 pulses were averaged within an integration time resulting in a significant RIN component in the total noise figure. The total noise power of the system can be written as follows:

$$\sigma_I^2 = \sigma_{\text{shot}}^2 + \sigma_{\text{thermal}}^2 + \sigma_{\text{RIN}}^2 + \sigma_{\text{DAQ}}^2, \quad (6)$$

where  $\sigma_{\text{shot}}^2$  is the signal-dependent shot noise power, which is the limiting noise component in an ideal heterodyne system,  $\sigma_{\text{thermal}}^2$  is the signal-independent thermal noise power that is inherent to the photodetector,  $\sigma_{\text{DAQ}}^2$  is the noise due to digitization of the signals, and  $\sigma_{\text{RIN}}^2$  is the excess noise due to the RIN of the SC. The SNR of the detected signal in the APD can be written as follows:

$$\text{SNR}(\text{dB}) = 10 \cdot \log\left(\frac{\mu_I}{\sigma_I}\right), \quad (7)$$

where  $\mu_I$  is the mean of the signal and  $\sigma_I$  is the standard deviation of the signal. The noise performance of the EXU-6 SC light source is shown in Fig. 4. The number of detected photons within an integration time was controlled using a fiber attenuator. The thermal noise was measured in the absence of any incident photons, and gradually, the number of photons was increased until the detectors reached 90% saturation. By including a 1 MHz low-pass filter with a very sharp cut-off, high-frequency noise is eliminated. At each moment, the mean and variance of the photocurrent measured by the detector were determined and plotted. Figure 4 shows that the unbalanced detection suffers from significant RIN contribution (dashed green and red lines). In our balanced detection scheme, the signals of detection module 1 were divided by the respective reference signals of detection module 2 to yield RIN corrected signals for each wavelength. Since OD was calculated as a ratio of two RIN corrected intensities at the same wavelength at different locations, the actual magnitude of the module 2 signals is divided out, so the OD does not depend on the actual magnitude of the module 2 signals. This method resulted in an additional SNR improvement due to RIN suppression. Around 5 dB improvement in SNR was achieved by using balanced detection and a 1 MHz low-pass filter. Figure 4 shows the improvement in SNR achieved by balanced detection for 500- and 600-nm wavelengths (dotted green and red lines).

### 2.4 Wavelength Sweep Hyperspectral Imaging

The acousto-optic tunable filter (Select, NKT Photonics A/S) used in the system (Fig. 3) allows to perform a wavelength

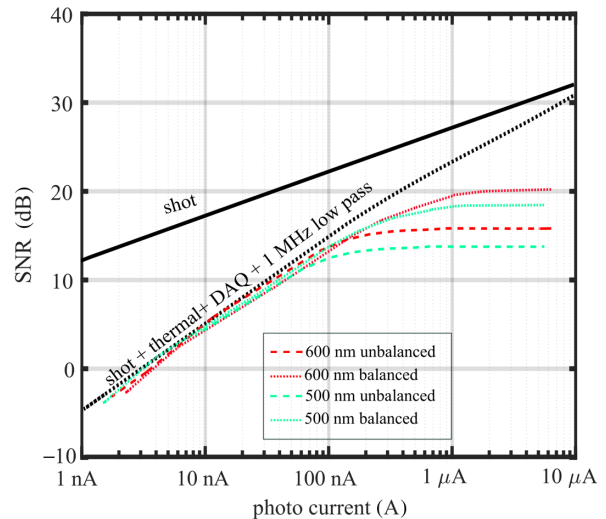


**Fig. 4** Noise performance of the SC source shown by plotting the SNR for different levels of mean signal in the photodetector for two wavelengths, 500 and 600 nm. The graph shows the theoretical shot noise limited SNR (solid black line) and the expected SNR due to the additional contribution of thermal and quantization noise to the shot noise (dotted black line). The measured SNR for two different wavelengths 500 and 600 nm is also shown (dashed green and red line, respectively). The SNR deteriorates for higher photocurrents because RIN noise scales as the square of detected photons in the photodetector. By using balanced detection, an improvement in SNR of  $\sim 5$  dB was achieved for these wavelengths (dotted green and red lines).

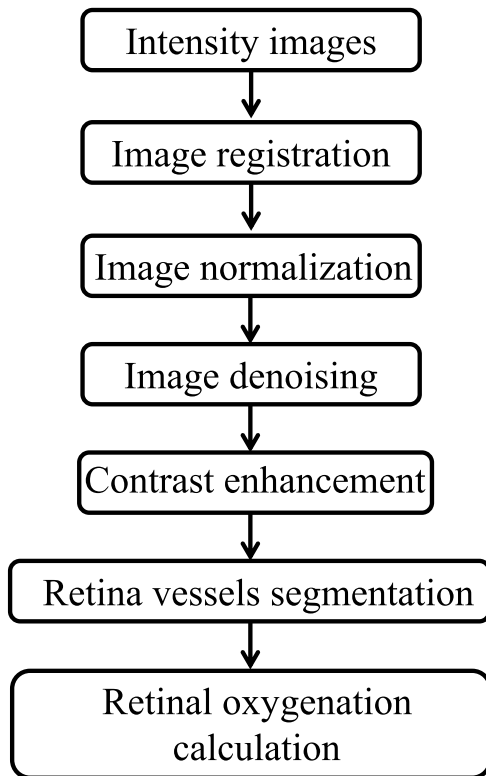


**Fig. 5** Pipeline for vessel segmentation and oxygenation extraction from retinal images.

sweep for the desired wavelength ranges between 450 and 650 nm and in desired steps (minimum step size 0.1 nm, maximum sweep speed of 10 wavelengths/s). We performed a wavelength sweep from 485 to 608 nm with the SLO with a step size in the wavelength of 3 nm and sweep speed of 1 step/s. Given that the imaging speed of our SLO is 10 fps, this enabled acquiring high-quality retinal images at a rate of 10 images/wavelength within 42 s of imaging. For these measurements, the dichroic filters D1, D2 and the clean-up filters CF2 and CF4 (see Fig. 3) were removed and only one channel was used in each detection unit.

### 2.5 In Vivo Human Measurements

The clinical pilot study obeyed the principles of the “Declaration of Helsinki” and was approved for human use by the medical ethical review board at the Amsterdam Universitair Medische Centra (VUmc location), Amsterdam. Tropicamide 0.5% wt./vol. drops were administered for pupil dilation during imaging. The optical power used for measuring human subjects was in agreement with the MPE established by the latest IEC standard 60825-1.<sup>32</sup> The laser safety considerations are detailed in Sec. 5. Different field-of-views (FoVs) could be implemented by changing the voltages provided to the scanners. Background measurements were taken prior to each imaging session and were subtracted from SLO images to remove artifacts, such as lens reflections. In order to utilize the full dynamic range of the detector, strong lens reflections from the last ophthalmic lens in the system were allowed to saturate the detector. All other stray reflections that did not saturate the detector were removed using the background measurements.

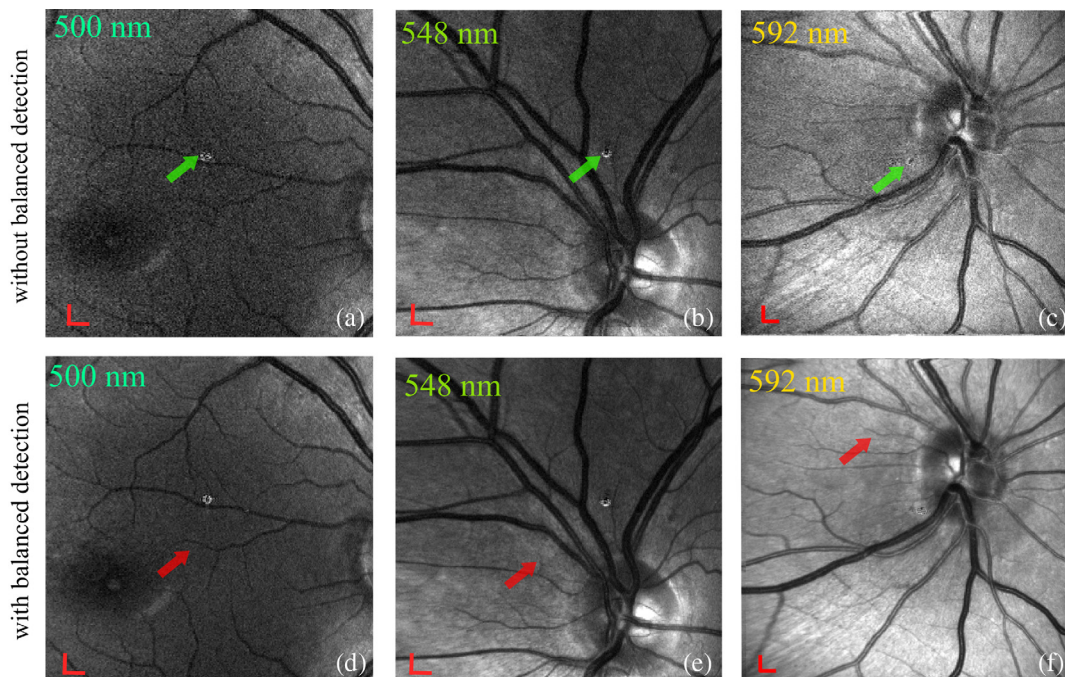


**Fig. 6** (a)–(e) Comparison of images with and without balanced detection—unaveraged retinal images from three different volunteers show the improvement in image quality due to balanced detection. The red arrows show the blood vessels that become visible only due to balanced detection. The green arrows point to the lens reflection artifact that saturated the detector and was not removed due to background subtraction. Scale bar represents 300  $\mu$ m in the retina.

## 2.6 Retinal Vessel Segmentation and Oxygenation Map

The SLO images were background corrected by performing a reference measurement before imaging *in vivo*. The background subtracted images were corrected for the sinusoidal scanning of the resonant scanner into a single image. The retinal oxygenation was constructed using the flow diagram shown in Fig. 5. First, several linear intensity images were registered using the scale-invariant feature transform method.<sup>41</sup> After correcting the images for translation, rotation, and affine transformations, an averaged image was constructed from the registered data. In order to segment and extract the vessels in the retinal image, the averaged image  $Im(x, y)$  was normalized as  $Im_N(x, y) = \frac{Im(x, y) - \min[Im(x, y)]}{\max[Im(x, y)] - \min[Im(x, y)]}$ , where min and max are defining the minimum and the maximum values in the registered and averaged image. Under the assumption that the SLO images have an approximate piecewise constant structure, the images were denoised using a total variation (TV) algorithm in order to preserve the vessel edges. Subsequently, contrast enhancement was applied to determine the blood vessel boundaries correctly. As has been shown by Davidoiu et al.,<sup>42</sup> a regularization TV model using a specialized fixed-point algorithm and isotropic TV norm improved the 2-D vasculature network segmentation for *ex-vivo* heart data. In our case, the regularization parameter in the TV algorithm has been fixed and chosen to be equal to the standard deviation of the normalized image and the convergence stopping parameter value has been set to 0.01. The contrast enhancement of the denoised image was performed using a method called contrast-limited adaptive histogram equalization.<sup>43</sup> Finally, the blood vessels detection and diameter calculation was performed using wavelets and edge location refinement.<sup>44</sup> The extracted vessel boundary coordinates were exported to MATLAB and were applied to the averaged image  $Im(x, y)$ . The extraction of the blood and tissue intensity values was done using the method described by Damodaran et al.<sup>26</sup>

## 3 Results and Discussion

### 3.1 Technical Aspects Regarding Multispectral SLO with an SC Source

#### 3.1.1 SNR improvement by balanced detection

Figure 6 shows the comparison between *in vivo* retinal images with and without balanced detection in three different volunteers with three different wavelengths. These images clearly show the improvement in image quality due to balanced detection. As described in Sec. 2.3, the RIN of the SC source was mitigated by using a balanced detection scheme. This resulted in an SNR improvement of 5 dB.

#### 3.1.2 Compensation for chromatic aberrations of the eye

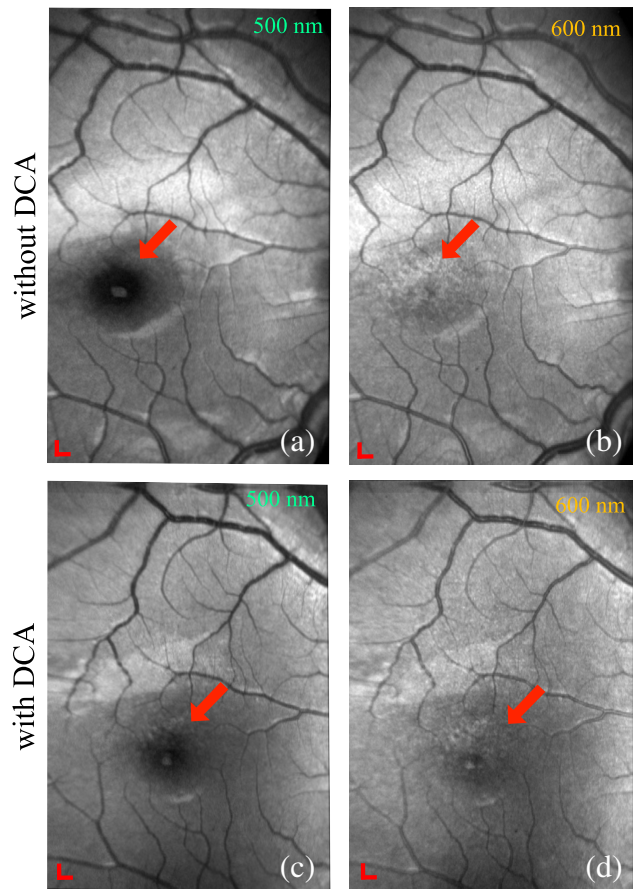
Chromatic aberrations in the human eye have been studied previously.<sup>45,46</sup> The longitudinal chromatic aberration (LCA) is a potential source of error in oximetry due to the dispersion in the human eye.<sup>37</sup> LCA causes the spatial location of each pixel in the multispectral image to be in a slightly different axial plane for different wavelengths. This effect can lead up to a 220  $\mu\text{m}$  longitudinal focal shift between the 498- and 594-nm wavelengths.<sup>47</sup> This effect can be corrected, as has been shown previously by others,<sup>48,49</sup> by using a DCL in the beam path.

Images acquired at 500 and 600 nm without the dispersion compensation lens (Fig. 7) in the right eye of a healthy human volunteer demonstrate that chromatic aberrations affect the multiwavelength SLO images; note the difference in the appearance of the foveal pit in the 500 nm and 600 nm images. This can be explained by a focal position that is at the depth of the foveal pit for the 600 nm image, and the 500 nm image has a shallower focus, as evidenced by the dark appearance of the foveal pit due to confocal gating. This focal separation between the different wavelengths was compensated by a dispersion compensation lens (Fig. 3) that resulted in the images [Figs. 7(c) and 7(d)] having a more uniform appearance of the foveal pit between the 500 and 600 nm channels. These images are similar to LCA-compensated images published by LaRocca et al.<sup>49</sup>

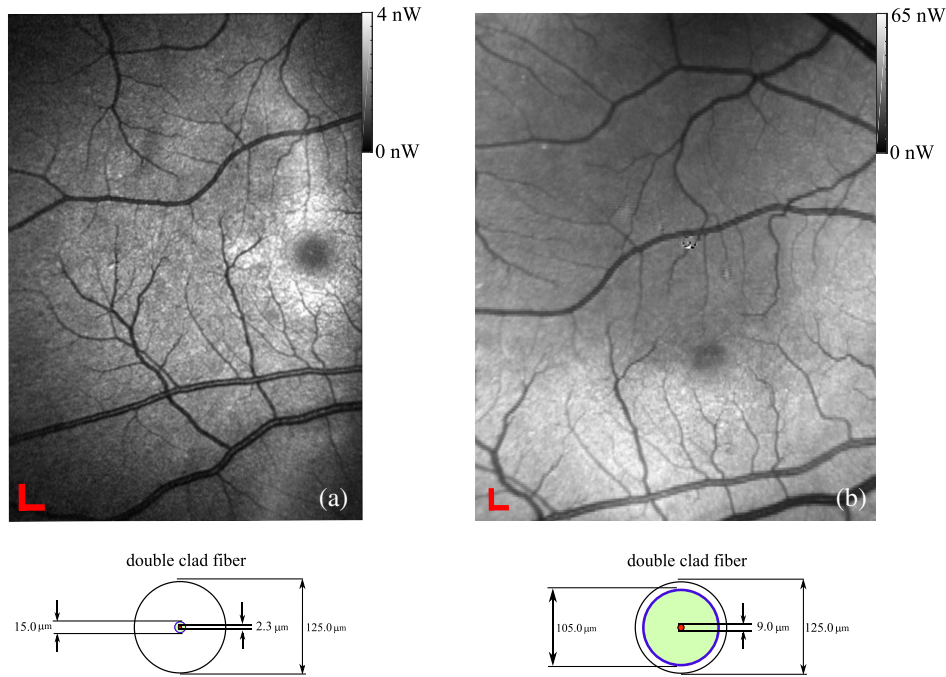
The transverse chromatic aberrations between the wavelengths were compensated in postprocessing of the images by applying a transformation metric, which aligns the images of different wavelengths to a chosen wavelength.

### 3.1.3 Effect of the size of the illumination and collection apertures of the DCF coupler

We determined the effect of using a DCF with different core and inner cladding diameters on throughput and sharpness of the



**Fig. 7** Images from the right eye of a human volunteer show the effect of LCA in the absence or presence of a dispersion compensation lens. The foveal pit (red arrows) appears more uniform in the images with dispersion compensation [panels (c) and (d)] compared to the images without dispersion compensation [panels (a) and (b)]. Scale bar represents 300  $\mu\text{m}$  in the retina.



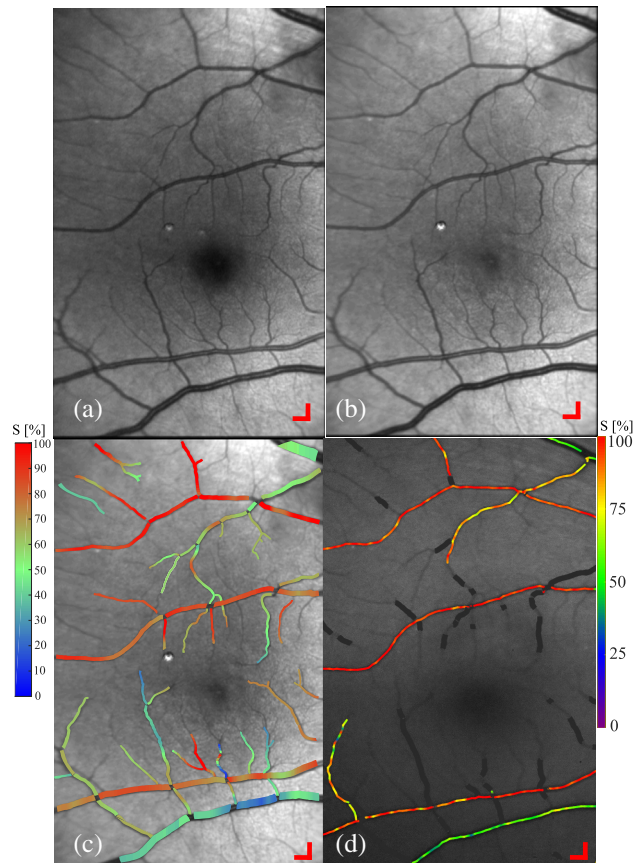
**Fig. 8** Unaveraged retinal SLO images (single frame each) from the described design in Sec. 2.2 with different DCFs. (a) DCF with a core 2.3  $\mu\text{m}$  diameter and an inner cladding of 15  $\mu\text{m}$ . (b) DCF with a core 9  $\mu\text{m}$  diameter and an inner cladding of 105  $\mu\text{m}$ . The cross-section of the DCF is shown in the bottom diagrams. Scale bar is 300  $\mu\text{m}$  in the retina.

image. DCF couplers with the same multimode fibers, but different DCFs (different core and inner cladding diameters) were used. Figure 8(a) shows an unaveraged SLO image of right eye of a healthy male volunteer imaged with a DCF having a core diameter of 2.3  $\mu\text{m}$  (single mode at 430 nm) and an inner cladding of compared with a DCF having a core diameter of 9  $\mu\text{m}$  and inner cladding diameter of 105  $\mu\text{m}$  [Fig. 8(b)]. The figures show that while the 2.3  $\mu\text{m}$ /15  $\mu\text{m}$  DCF gives images with sharper appearance, this comes at the cost of throughput, as indicated by the intensity scale bars. For subdiffuse measurements with higher throughput requirements for fast quantitative imaging, the 9  $\mu\text{m}$ /105  $\mu\text{m}$  DCF is better suited since the amount of averaging required to achieve an SNR of 20 dB is smaller than for the 2.3  $\mu\text{m}$ /15  $\mu\text{m}$  DCF.

### 3.2 In Vivo Two Wavelength Oximetry

Retinal oximetry was demonstrated in two healthy volunteers using the optimal two wavelengths, 498 and 594 nm. Figures 9(a) and 9(b) show the retinal images at 498 and 594 nm, respectively. After vessel segmentation and analysis, as described in Sec. 2.6, an oxygen saturation map of the blood vessels was created and overlaid on the 594 nm image, as shown in Fig. 9(c). Figure 9(d) shows an image taken with the Oxymap Tx for comparison. Similar measurements were made in volunteer 2, as shown in Fig. 10. The smallest vessels for which oxygen values are provided are 40  $\mu\text{m}$  in diameter.

To analyze the repeatability of the oxygenation measurements, volunteer 1 was imaged three times with 8-min interval in between the measurements. The average oxygenation in four vessels (vessels 1 to 3: arteries; vessel 4: vein) is shown in Fig. 11. The calculated oxygenation values in these vessels reproduce very well, despite the difference in positioning of the eye between the three imaging sessions, resulting in different



**Fig. 9** SLO images taken from a healthy human volunteer at two wavelengths, (a) 498 nm and (b) 594 nm. Ten frames were registered and averaged to improve the SNR of the images. (c) The estimated oximetry results are shown. (d) The image acquired using Oxymap Tx ehf is shown for comparison. Scale bar represents 300  $\mu\text{m}$  in the retina.

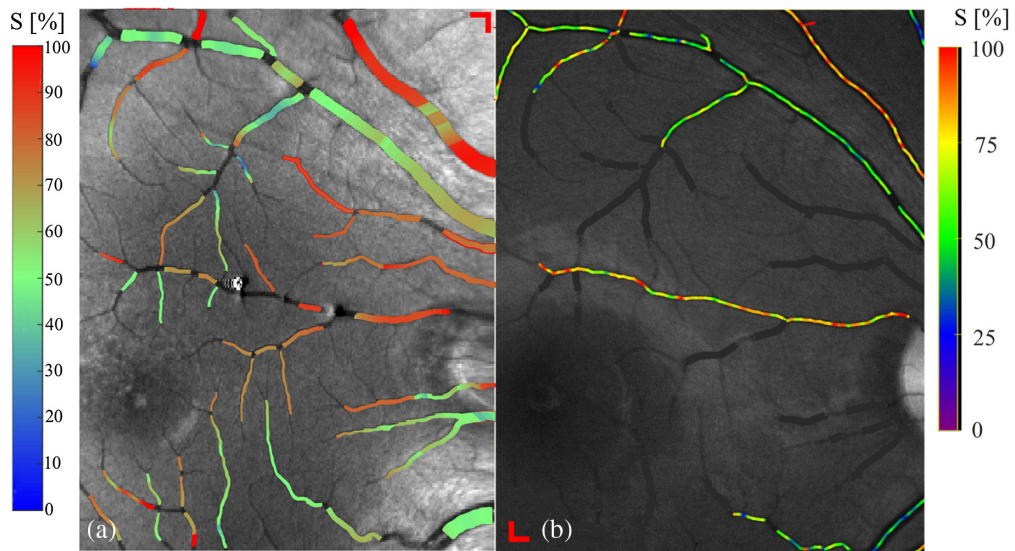


**Fig. 10** (a) Estimated oxygenation values in volunteer 2 and (b) corresponding image by Oxymap Tx. Scale bar represents 300  $\mu\text{m}$  in the retina.

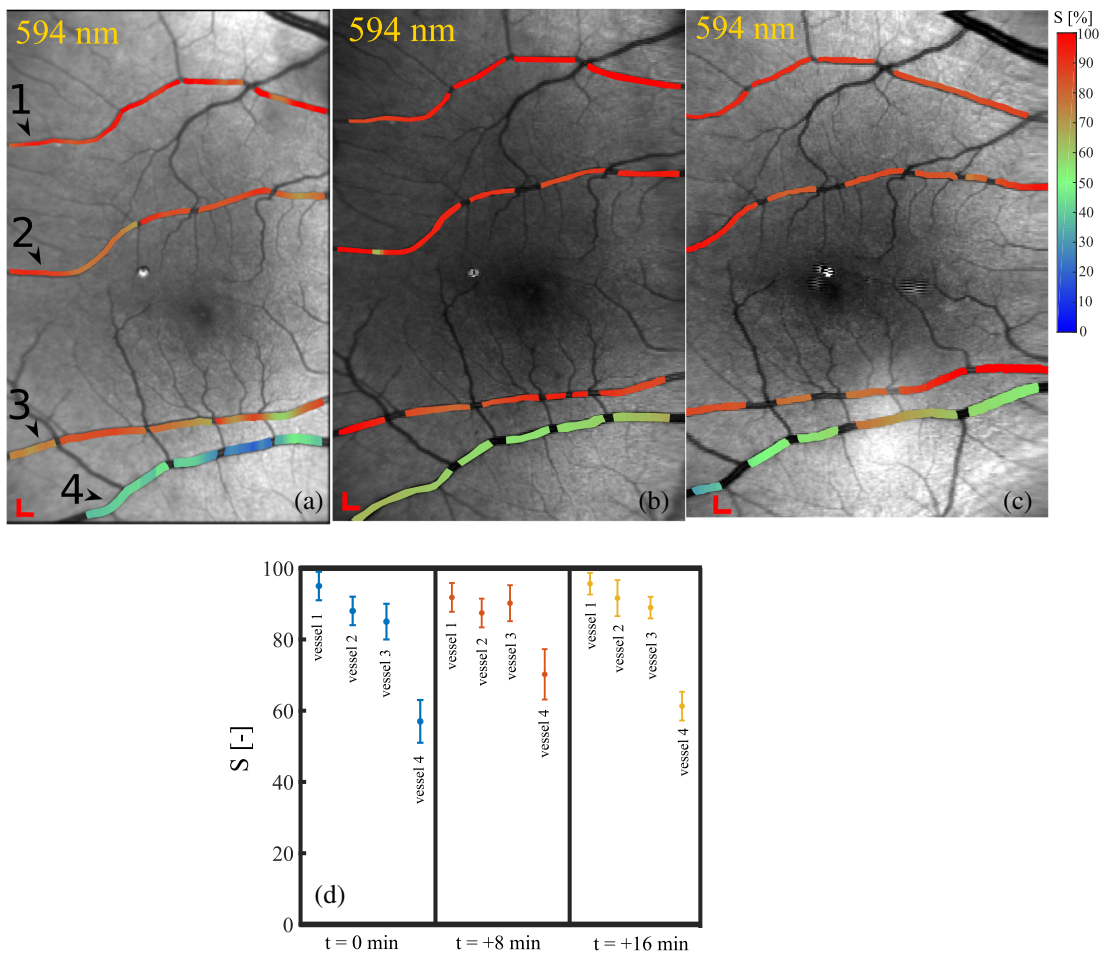


**Fig. 11** Retinal imaging was performed in volunteer 1 with an interval of 8 min to study the repeatability of the measurements. (a)–(c) Measurements made at 0, 8, and 16 min in volunteer 1 with the calculated oximetry for three large arteries and a vein. Scale bar represents 300  $\mu\text{m}$ . The numerical values are plotted in (d).

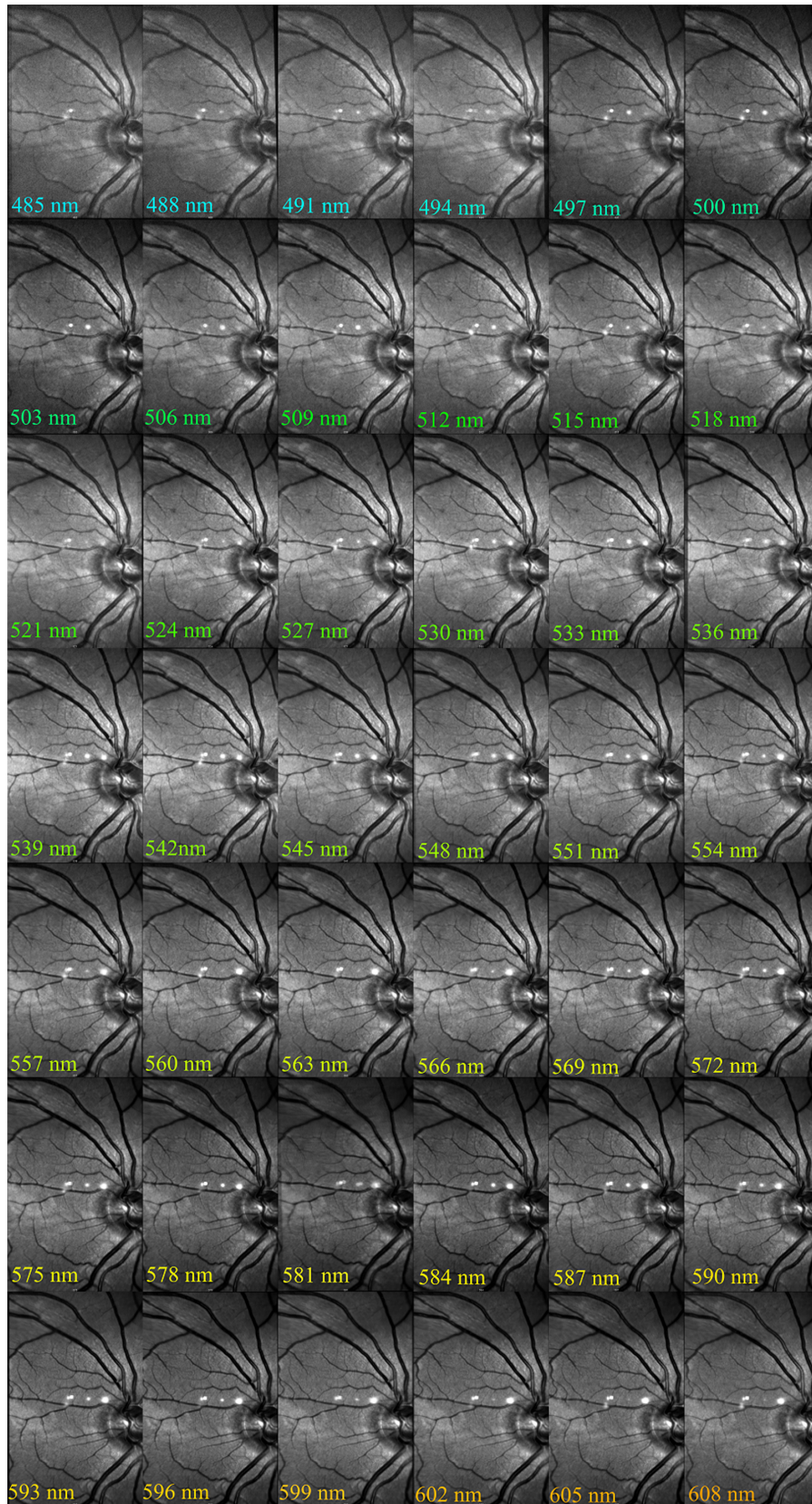


**Fig 12** Wavelength sweep from 485 to 608 nm.

overall intensity levels and differences in focus depth, as evidenced by the different appearance of the foveal pit across the three sessions.

### 3.3 Wavelength Sweep Hyperspectral Imaging

Similar to other SLO systems, the system described in Fig. 3 can image different sections of the retina at high frame rates, but the SC source used in our system also has the advantage of imaging at any desired wavelength and to sweep wavelengths in selected ranges and steps in the 484 to 700 nm range. Figure 12 shows the *in vivo* result of a wavelength sweep from 485 to 608 nm performed in volunteer 2. The measurement took 42 s to complete, and each wavelength image shown in the figure was registered to the first frame of that wavelength and averaged in postprocessing. As a result of the balanced detection and well-fixated eye of the volunteer, the images exhibit good contrast.

Six blood vessels providing a wide range of vessel diameters were selected from the spectral cube, and the OD values were

obtained for these vessels after performing the vessel segmentation in individual images. The weighted mean and the standard deviation (weights = 1/standard error) were obtained for these vessels and Eq. (1) (where  $G$  was assumed to be 0 and the blood hemoglobin concentration was assumed to be 15 g/dL) was used as the model to perform a weighted fit the OD values in order to extract the  $\langle L_{\text{eff}} \rangle$  and  $S$  values, as shown in Fig. 13. The  $S$  values of these vessels are similar to the values obtained by dual-wavelength imaging of the same volunteer (Fig. 10) and oxygen saturation maps obtained with Oxymap Tx ehf. The errors on the fitted parameters were calculated from the diagonals of the covariance matrix.<sup>50</sup> From the fitted values of  $\langle L_{\text{eff}} \rangle$ , the relationship between  $\langle L_{\text{eff}} \rangle$  and  $D_{\text{ves}}$  for these vessels ( $D_{\text{ves}} \geq 70 \mu\text{m}$ ) could be established, and this relationship is plotted in Fig. 14. The relation between  $\langle L_{\text{eff}} \rangle$  and  $D_{\text{ves}}$  was found to be fitted well by a linear function,  $\langle L_{\text{eff}} \rangle (\mu\text{m}) = (0.46 \cdot D_{\text{ves}} + 5.2) \pm 6.0 (\mu\text{m})$ , where  $\langle L_{\text{eff}} \rangle$  and  $D_{\text{ves}}$  are given in micrometers. From this relationship, we conclude that our subdiffuse SLO imaging scheme, where a small illumination spot is used in combination with a large collection aperture,

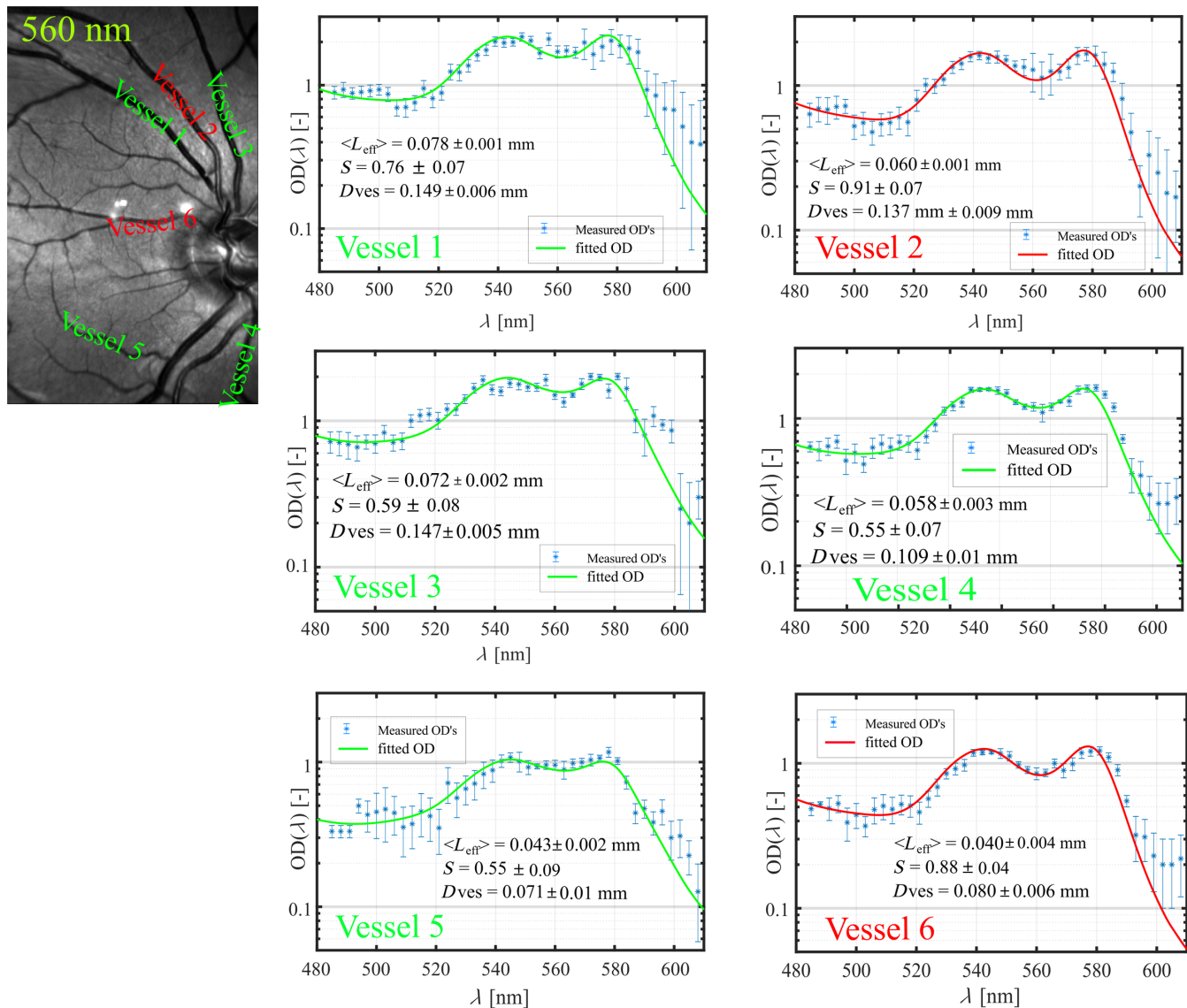
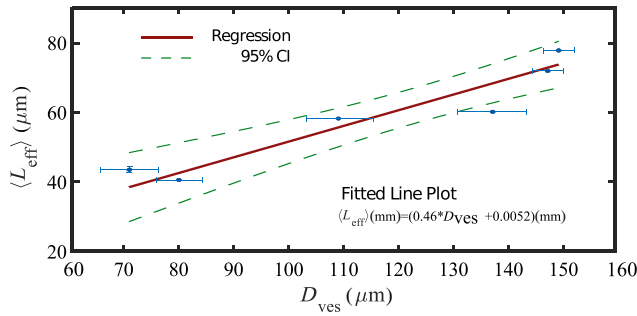


Fig. 13 Plot of OD as a function of wavelength for six blood vessels in the right eye of a healthy volunteer.



**Fig. 14** Linear regression fit of the effective path length  $\langle L_{\text{eff}} \rangle$  as a function of the blood vessel diameter  $D_{\text{ves}}$ .

works in a light transport regime between a fundus camera (where  $\langle L_{\text{eff}} \rangle = D_{\text{ves}}$ ) and a truly confocal SLO, where  $\langle L_{\text{eff}} \rangle = \langle L_{\text{bs}} \rangle$  with  $\langle L_{\text{bs}} \rangle$  is the backscatter path length, which is not expected to have a linear dependence on  $D_{\text{ves}}$ . We expect that the exact relation between  $\langle L_{\text{eff}} \rangle$  and  $D_{\text{ves}}$  depends on the details of the measurement geometry and will, for example, be different for different DCF cladding sizes or, equivalently, for different confocal aperture sizes. Furthermore, we have here in our fits assumed  $\langle L_{\text{eff}} \rangle$  to be wavelength independent, whereas it is expected that  $\langle L_{\text{eff}} \rangle$  depends on the scattering and absorption coefficients of blood and is, therefore, in reality, wavelength dependent. This is a topic for future investigations.

One notable advantage of the wavelength sweep using the SLO is the availability of the spectral properties of the entire retina for multiple wavelengths. This will be in the future permit expansion of the diagnostic capabilities of an SLO by providing spectral fingerprints of additional chromophores such as carotenoids. However, the imaging speed of the wavelength sweep should be dramatically improved before the clinical implementation of wavelength sweeping would become feasible.

## 4 Conclusion

In conclusion, we have demonstrated *in vivo* human retinal imaging with an SLO based on a SC source. The RIN noise of the illumination source has been addressed by implementing balanced detection. The balanced detection increased the SNR and, therefore, improved the image quality and accuracy of oximetry calculations. The implementation of an achromatizing lens reduced the effect of chromatic aberrations introduced by the human eye, although this did not have a large effect on saturation estimation. The use of a DCF with large inner cladding provided the best trade-off between image contrast and SNR. This allowed for high-resolution *in vivo* visualization of the oxygenation of retinal blood vessels in healthy volunteers. The oxygen saturation of the larger vessels of the retinas of two human volunteers was in agreement with the Oxymap-derived saturations; in addition, our SLO system was able to provide oxygen saturation in much smaller vessels. The saturation measured in three different imaging sessions of the same volunteer (8 min apart) demonstrated the reproducibility of our measurements. Finally, by performing a wavelength sweep between 485 and 608 nm, we determined an approximately linear relationship between the effective path length of photons through the blood vessels and vessel diameter for our SLO geometry that employs a DCF with a large inner cladding. It is expected that our SLO will be a valuable tool to study the effect of degenerative retinal diseases on the oxygenation in the retinal microvasculature.

## 5 Appendix: Laser safety calculations

Calculations for the MPE on the retina were done using the latest laser safety standard IEC 60825-1 published in 2014.<sup>32</sup> The most conservative estimate of the MPE can be obtained by assuming a collimated, static beam entering the eye. A limiting aperture (LA) to determine MPE for the eye was taken to be 7 mm (diameter). A 7-mm LA equals an area of  $3.85 \times 10^{-5} \text{ (m}^2\text{)}$ . The accessible emission limit (AEL) was then calculated as follows:

$$\text{AEL} = \text{MPA} \times \text{LA}. \quad (8)$$

From the IEC standard, the MPE expressed as irradiance or radiant exposure for the wavelength range of 450 to 650 nm for a collimated beam  $C_6 = 1$  with the exposure time of 10 s or longer is given by

$$\text{AEL} = \begin{cases} 10^{0.02 \cdot (\lambda - 450)} (\text{W m}^{-2}) \times 3.85 \times 10^{-5} (\text{m}^2) & 450 \leq \lambda \leq 500 \\ 10 (\text{W m}^{-2}) \times 3.85 \times 10^{-5} (\text{m}^2) & 500 \leq \lambda \leq 700 \end{cases}$$

However, the resonant, galvo scanning is performed within the whole FoV, which makes this AEL estimation very conservative. If the illumination of the retina is assumed to be what the standard calls extended the source, the AEL limit will be more than an order of magnitude higher. Significant increases in AEL can also be obtained by limiting each imaging session to less than 10 s/day. When combining multiple wavelengths, the following criterion should be met:

$$\sum_{n=1}^N \frac{P(\lambda_n)}{\text{AEL}(\lambda_n)} \leq 1, \quad (9)$$

where  $P$  is the applied power per wavelength and  $N$  is the total number of simultaneous wavelengths. Depending on the AEL and the detector sensitivity, the ratio of  $P$  and AEL was chosen for optimum image quality. For the wavelength sweep, the applied power at each wavelength was ensured to be always less than the limit imposed by Fig. 15. The total time of the sweep was 42 s, which is far less than the radiation window of 30,000 s for safe exposure.

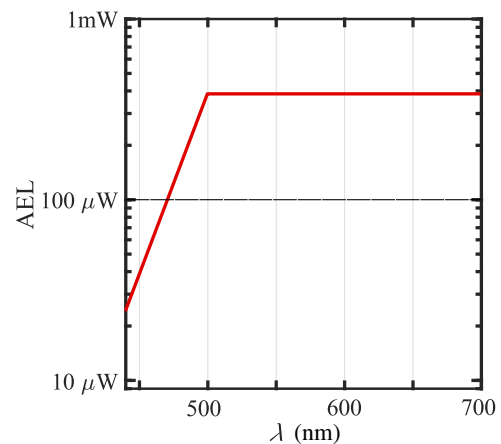


**Fig. 15** AEL for different wavelengths in 450 to 650 nm considering a collimated static beam for 30,000 s.

## Disclosures

M.D. has financial interest in VU Amsterdam (P), A.A. has financial interest in VU Amsterdam (P) and TNO (P), J.F.B. has financial interest in VU Amsterdam (P) and Heidelberg Engineering GmbH (F).

## Acknowledgments

This research is funded by the Netherlands Organization for Scientific Research (NWO) with a Vici (J.F.B.) grant (918.10.628), the Netherlands Organization for Health Research and Development ZonMW (Grant No. 91212061), which is a part of NWO, and Heidelberg Engineering GmbH.

## References

- N. D. Wangsa-Wirawan and R. Linssenmeier, "Retinal oxygen: fundamental and clinical aspects," *Arch. Ophthalmol.* **121**(4), 547–557 (2003).
- T. Bek, E. Stefansson, and S. H. Hardarson, "Retinal oxygen saturation is an independent contributor to the severity of retinopathy in diabetic patients," *Br. J. Ophthalmol.* **103**(8), 1167–1172 (2018).
- E. D. Cole et al., "Contemporary retinal imaging techniques in diabetic retinopathy: a review," *Clin. Exp. Ophthalmol.* **44**(4), 289–299 (2016).
- R. Klein et al., "Diabetic retinopathy as detected using ophthalmoscopy, a nonmydriatic camera and a standard fundus camera," *Ophthalmology* **92**, 485–491 (1985).
- G. Michelson, M. Scibor, and D. Schweitzer, "Intravascular oxygen saturation in retinal vessels in normal subjects and open-angle glaucoma subjects," *Invest. Ophthalmol. Visual Sci.* **84**(3), 289–295 (2006).
- A. Geirsdottir et al., "Retinal oxygen metabolism in exudative age-related macular degeneration," *Acta Ophthalmol.* **92**(1), 27–33 (2014).
- O. B. Olafsdottir et al., "Retinal oximetry in primary open-angle glaucoma," *Invest. Ophthalmol. Visual Sci.* **52**(9), 6409–6413 (2011).
- E. Nitta et al., "Retinal oxygen saturation before and after glaucoma surgery," *Acta Ophthalmol.* **95**(5), e350–e353 (2016).
- S. Rílvén, T. L. Torp, and J. Grauslund, "Retinal oximetry in patients with ischaemic retinal diseases," *Acta Ophthalmol.* **95**(2), 119–127 (2017).
- A. B. Einarsdottir et al., "Retinal oximetry imaging in Alzheimer's disease," *J. Alzheimer's Dis.* **49**(1), 79–83 (2015).
- N. J. Hart et al., "Ocular indicators of Alzheimer's: exploring disease in the retina," *Acta Neuropathol.* **132**(6), 767–787 (2016).
- A. B. Einarsdottir et al., "Retinal oximetry is affected in multiple sclerosis," *Acta Ophthalmol.* **96**(5), 528–530 (2018).
- T. Shiba, K. Maruo, and T. Akahoshi, "Development of a multi-field fundus photographing system using a non-mydriatic camera for diabetic retinopathy," *Diabetes Res. Clin. Pract.* **45**(1), 1–8 (1999).
- E. DeHoog and J. Schwiegerling, "Optimal parameters for retinal illumination and imaging in fundus cameras," *Appl. Opt.* **47**(36), 6769–6777 (2008).
- A. Geirsdottir et al., "Retinal vessel oxygen saturation in healthy individuals," *Invest. Ophthalmol. Visual Sci.* **53**(9), 5433–5442 (2012).
- J. C. Ramella-Roman et al., "Measurement of oxygen saturation in the retina with a spectroscopic sensitive multi aperture camera," *Opt. Express* **16**(9), 6170–6182 (2008).
- D. J. Mordant et al., "Spectral imaging of the retina," *Eye* **25**(3), 309–320 (2011).
- B. Khoobehi, J. M. Beach, and H. Kawano, "Hyperspectral imaging for measurement of oxygen saturation in the optic nerve head," *Invest. Ophthalmol. Visual Sci.* **45**(5), 1464–1472 (2004).
- W. R. Johnson et al., "Snapshot hyperspectral imaging in ophthalmology," *J. Biomed. Opt.* **12**(1), 014036 (2014).
- R. A. Ashman, F. Reinholz, and R. H. Eikelboom, "Oximetry with a multiple wavelength SLO," *Int. Ophthalmol.* **23**(4–6), 343–346 (2001).
- H. Li et al., "Measurement of oxygen saturation in small retinal vessels with adaptive optics confocal scanning laser ophthalmoscopy," *J. Biomed. Opt.* **16**(11), 110504 (2011).
- S. P. Chong et al., "Structural and functional human retinal imaging with a fiber-based visible light OCT ophthalmoscope," *Biomed. Opt. Express* **8**(1), 323–337 (2017).
- L. E. MacKenzie et al., "In vivo oximetry of human bulbar conjunctival and episcleral microvasculature using snapshot multispectral imaging," *Exp. Eye Res.* **149**, 48–58 (2016).
- J. P. Campbell et al., "Detailed vascular anatomy of the human retina by projection-resolved optical coherence tomography angiography," *Sci. Rep.* **7**, 1–11 (2017).
- S. Pi et al., "Rodent retinal circulation organization and oxygen metabolism revealed by visible-light optical coherence tomography," *Biomed. Opt. Express* **9**(11), 5851–5862 (2018).
- M. Damodaran, A. Amelink, and J. F. de Boer, "Optimal wavelengths for subdiffuse scanning laser oximetry of the human retina," *J. Biomed. Opt.* **23**(08), 086003 (2018).
- A. Sassaroli and S. Fantini, "Comment on the modified Beer-Lambert law for scattering media," *Phys. Med. Biol.* **49**(14), N255 (2004).
- L. Kocsis, P. Herman, and A. Eke, "The modified Beer-Lambert law revisited," *Phys. Med. Biol.* **51**(5), N91–N98 (2006).
- N. Rajaram et al., "Experimental validation of the effects of microvasculature pigment packaging on *in vivo* diffuse reflectance spectroscopy," *Lasers Surg. Med.* **42**(7), 680–688 (2010).
- J. C. Finlay and T. H. Foster, "Effect of pigment packaging on diffuse reflectance spectroscopy of samples containing red blood cells," *Opt. Lett.* **29**(9), 965–967 (2004).
- D. Schweitzer et al., "In vivo measurement of the oxygen saturation of retinal vessels in healthy volunteers," *IEEE Trans. Biomed. Eng.* **46**(12), 1454–1465 (1999).
- International Electrotechnical Commission, "International Electrotechnical Commission, Safety of Laser Products Part 1: Equipment Classification and Requirements, (Geneva, Switzerland), IEC-60825-1 (2014)," **122** (2014).
- Thorlabs GmbH, *APD410x Operation Manual*, Thorlabs GmbH, Germany (2015).
- S. Lemire-Renaud et al., "Double-clad fiber coupler for endoscopy," *Opt. Express* **18**(10), 9755–64 (2010).
- E. D. Montigny et al., "Double-clad fiber coupler for partially coherent detection," *Opt. Express* **23**(7), 9040–9051 (2015).
- W. J. Donnelly and A. Roorda, "Optimal pupil size in the human eye for axial resolution," *J. Opt. Soc. Am. A* **20**(11), 2010–2015 (2003).
- M. Vinas et al., "Longitudinal chromatic aberration of the human eye in the visible and near infrared from wavefront sensing, double-pass and psychophysics," *Biomed. Opt. Express* **6**(3), 948–962 (2015).
- I. B. Gonzalo, R. D. Engelsholm, and O. Bang, "Noise study of all-normal dispersion supercontinuum sources for potential application in optical coherence tomography," *Proc. SPIE* **10591**, 105910C (2018).
- G. McConnell, "Noise analysis of a white-light supercontinuum light source for multiple wavelength confocal laser scanning fluorescence microscopy," *J. Phys. D: Appl. Phys.* **38**(15), 2620–2624 (2005).
- J. M. Dudley et al., "Fundamental noise limitations on supercontinuum generation in microstructure fiber," *Phys. Rev. Lett.* **90**(11), 113904 (2003).
- D. G. Lowe, "Distinctive image features from scale-invariant keypoints," *Int. J. Comput. Vision* **60**(2), 91–110 (2004).
- V. Davidoiu et al., "Evaluation of noise removal algorithms for imaging and reconstruction of vascular networks using micro-CT," *Biomed. Phys. Eng. Express* **2**(4), 45015 (2016).
- K. Zuiderveld, "Contrast limited adaptive histogram equalization," in *Graphics Gems IV*, P. S. Heckbert, Ed., ch. Contrast L, pp. 474–485, Academic Press Professional, Inc., San Diego, California (1994).
- P. Bankhead et al., "Fast retinal vessel detection and measurement using wavelets and edge location refinement," *PLoS One* **7**(3), e32435 (2012).
- D. A. Atchison and G. Smith, *Optics of the Human Eye*, Butterworth-Heinemann, Oxford (2000).
- E. J. Fernández et al., "Chromatic aberration correction of the human eye for retinal imaging in the near infrared," *Opt. Express* **14**(13), 6213–6225 (2006).
- R. J. Zawadzki et al., "Ultrahigh-resolution optical coherence tomography with monochromatic and chromatic aberration correction," *Opt. Express* **16**(11), 8126–8143 (2008).
- S. P. Chong et al., "Ultrahigh resolution retinal imaging by visible light OCT with longitudinal achromatization," *Biomed. Opt. Express* **9**(4), 1477–1491 (2018).

49. F. LaRocca et al., "True color scanning laser ophthalmoscopy and optical coherence tomography handheld probe," *Biomed. Opt. Express* **5**(9), 3204–3216 (2014).
50. A. Amelink, D. J. Robinson, and H. J. C. M. Sterenborg, "Confidence intervals on fit parameters derived from optical reflectance spectroscopy measurements," *J. Biomed. Opt.* **13**(5), 054044 (2008).

**Mathi Damodaran** is a PhD candidate in the Biophotonics and Medical Imaging Group, Vrije Universiteit Amsterdam. He received his Bachelor of Engineering degree in electronics and communication from Anna University, Chennai (India). He received his MSc degree in photonics from the University of St. Andrews, Scotland, in a joint program with Universiteit Gent, Belgium. The focus of his research is developing optical imaging techniques for diagnosis and follow-up of the retinal diseases. He is currently working at Philips Research, Eindhoven. He is a member of SPIE.

**Arjen Amelink** received his master's degree in experimental physics from the University of Groningen in 1995 and his PhD in atomic physics from the University of Utrecht in 2000. After one year at Philips Research, he started in 2001 as a postdoc at the Center for Optical Diagnostics and Therapy (CODT) at the Erasmus Medical Center in Rotterdam. From 2005 to 2013, he was an assistant professor at the CODT, where his research focused on clinical applications of optical spectroscopic technologies. Since 2014, he has been a senior scientist at the Medical Photonics Research Program within TNO.

**Fabio Feroldi** is a PhD candidate in the Biophotonics and Medical Imaging Group, Vrije Universiteit Amsterdam. He received his bachelor's degree in physics from the University of Bologna (Italy), and his master's degree in medical physics from Vrije Universiteit Amsterdam. His research is aimed at developing novel endoscopic optical imaging techniques for diagnosing internal organs. He is currently affiliated with the University of California Berkeley, where

he develops optical systems that detect physiological signals in the retina.

**Benjamin Lochocki** is a postdoc at the LaserLab, Vrije Universiteit of Amsterdam. He studied photonics and image processing at the University of Applied Science in Darmstadt. He received his PhD in biomedical optics from the University College Dublin in 2014. His interests include optical imaging techniques, such as single-pixel imaging, computational imaging, and the development of optical devices for ophthalmic applications as well as Raman spectroscopy of diseased tissue.

**Valentina Davidoiu** was a research associate in the Biophotonics and Medical Imaging Group, Vrije Universiteit Amsterdam and Rotterdam Ophthalmic Institute, Rotterdam Eye Hospital. She received her bachelor's degree from Politehnica University, Bucharest (Romania). She received her MSc degree in signal processing from Politehnica University, Bucharest (Romania), in a joint program with TELECOM ParisTech, France. She received her PhD in signal processing and computer science at INSA Lyon, France, in a joint project with ESRF, Grenoble, France. After her PhD, she was a research associate in a joint project between King's College London and Oxford University. The focus of her research is developing an algorithm for image reconstruction and segmentation. She is currently a scientist at Philips Research Europe, Eindhoven.

**Johannes F. de Boer** is a full professor in the Department of Physics and Astronomy, VU University, Amsterdam and a former director of LaserLaB Amsterdam. He has been an active researcher in biomedical optics for over 20 years since obtaining his PhD from the University of Amsterdam. He was an assistant professor at the Beckman Laser Institute, UC Irvine, California, and an associate professor at Harvard Medical School, Boston, Massachusetts. He is a member of SPIE and an OSA fellow.